Int. J. Electrochem. Sci., 14 **(2019)** 9181 – 9192, doi: 10.20964/2019.09.62

International Journal of
ELECTROCHEMICAL
SCIENCE
www.electrochemsci.org

Corrosion Behavior of X100 Pipeline Steel and Its Heat-Affected Zones in Simulated Alkaline Soil Solution

Xinhua Wang[1], *Yang yong* [1,2,*], *Yingchun Chen*[1], *Haitao Wang*[2], *Kailin Wei*[1]

[1] College of Mechanical Engineering and Applied Electronics Technology, Beijing University of Technology, Beijing 100024, China
[2] China Special Equipment Inspection and Research Institute, Beijing 100029,China
[*]E-mail: iyangyong@sohu.com

Received: 13 May 2019 / *Accepted:* 1 July 2019 / *Published:* 5 August 2019

The microstructure changes underwent by the heat-affected zones (HAZ) of a X100 pipeline steel and the corrosion behavior of these zones and the base steel were studied in a simulated alkaline soil solution. The coarse-grained heat-affected zone （CGHAZ） and the intercritically reheated coarse-grained heat-affected zone (ICCGHAZ) were simulated by a Gleeble thermomechanical processing machine with different thermal cycle times, peak temperatures, and cooling rates. Open circuit potential (OCP), potentiodynamic polarization, electrochemical impedance spectroscopy (EIS), and scanning electron microscopy (SEM) were used to characterize the corrosion behavior of the X100 pipeline steel and its CGHAZ and ICCGHAZ in a simulated alkaline soil solution. The microstructures of the CGHAZ and ICCGHAZ were found to be significantly different than that of the base steel. The X100 base steel showed the most positive OCP, the lowest corrosion current density, and the largest polarization resistance. In contrast, the ICCGHAZ showed the most negative OCP, the highest corrosion current density, and the lowest polarization resistance. The CGHAZ and ICCGHAZ underwent corrosion to a higher extent compared to base steel after immersion in a simulated soil solution for similar periods of time. Those samples containing HAZ and base steel were found to present significant galvanic corrosion. The CGHAZ and ICCGHAZ of a X100 pipeline steel immersed in a simulated alkaline soil solution exhibited lower corrosion resistance than the base steel.

Keywords: X100 steel; heat-affected zones; corrosion behavior; simulated alkaline soil solution; electrochemical impedance

1. INTRODUCTION

Owing to the strong demand for petrochemical energy in recent years, high-strength, large-diameter and high-pressure transmission pipelines are the inevitable development trend for oil and gas

[1, 2]. The utilization of high-strength pipeline steel can significantly reduce construction and operating costs of long-distance oil and gas pipelines [3, 4]. The development and utilization of X100 high-strength pipes has become a hot topic, and researchers have conducted pilot tests and confirmed that X100 pipeline steel meets relevant technical specifications [5, 6]. Northwest China is an important hub of oil and gas transmission pipelines. The Korla soil found in this area is the typical desert alkaline soil with high salinity, low humidity, and good air permeability, and a pH of ca. 8.3–9.4, which make it extremely corrosiveness to buried pipelines [7, 8].

External corrosion is one of the main potential risks of buried oil and gas pipelines. The different microstructure and microcomposition of the heat-affected zone (HAZ), the base steel, and the weldment at the welding zones increases the likelihood of dangerous ruptures in pipelines [9]. As revealed in previous studies [10–17], the microstructure of the HAZ has an important influence on the corrosion behavior of pipeline steel, although this influence depends on the types of steel and the corrosion environments. LIU [10] conducted corrosion electrochemical experiments on a X60 pipeline steel immersed in two different solutions and found superior corrosion resistance on the HAZ versus the base steel in an active dissolution state. In contrast, the base steel showed higher corrosion resistance than the HAZ when a corrosion product film was formed on the steel surface. Fan [11] reported higher corrosion rates for the HAZ of an X70 pipeline steel in seawater compared to the base steel. Mohammadi [12] reported lower corrosion current densities in an acidic solution for the HAZ of an X80 pipeline steel compared to the base steel, while the corrosion current density in an alkaline solution was higher than that of the base steel. Zhao [13] reported lower corrosion resistance of the coarse-grained HAZ (CGHAZ) of an X80 pipeline steel in a near-neutral chloride solution versus the fine-grained HAZ (FGHAZ) and the base steel, which can be attributed to the coarse microstructure. Shi [14] reported very low corrosion resistance for the intercritically reheated CGHAZ (ICCGHAZ) of an X80 pipeline steel immersed in a 5.0 wt% NaCl solution saturated with carbon dioxide (CO_2) because of the presence of coarse necklace-shaped M/A constituents and high-carbon martensite. Zhang [15] reported lower corrosion rates for the welded joint zone (i.e., weldment and HAZ) of an X100 pipeline steel compared to the base metal in an acidic environment. Eliyan [16,17] studied the corrosion behavior of HAZs with different microstructures by simulating the effect of different cooling temperatures of an X100 pipeline steel in a dilute bicarbonate solution. These authors found the microstructure had a significant influence on the passivation process, passivation current, and the corrosion product film formation.

The microstructure and properties of CGHAZ and ICCGHAZ have been widely studied [18–20]. These characteristics play an important role in the safety of the welded joints present in pipelines. However, the corrosion behavior of CGHAZ and ICCGHAZ of an X100 pipeline steel in an alkaline soil environment has been scarcely studied. In this work, the CGHAZ and ICCGHAZ of an X100 pipeline steel were simulated by a Gleeble thermomechanical processing machine under different thermal cycle times, peak temperatures, and cooling rates. Electrochemical corrosion measurements and surface analysis were carried out to determine the effects of different microstructures on the corrosion behavior of an X100 pipeline steel in a simulated Korla alkaline solution.

2. EXPERIMENTAL

2.1 Materials and solutions

The testing specimens were cut from an API X100 pipeline steel plate with a chemical composition (wt%): C 0.051, Mn 1.909, Si 0.216, P 0.010, S 0.004, Cr 0.287, Ni 0.313, Cu 0.139, Al 0.045, Mo 0.250, Ti 0.012, Nb 0.063, V 0.039, Pb 0.002, B 0.0003, Sn 0.003, and As 0.005 (Fe balance).

A Gleeble 3180 thermal simulation machine (DSI, USA) was used to simulate the CGHAZ and ICCGHAZ under repetitve thermal cycles as represented in Figure 1 [3]. To simulate the CGHAZ microstructures, the samples were firstly heated at 130 °C/s up to 1300 °C, maintained for 1 s at this temperature, cooled down to 800 °C with a controlled rate of 80 °C /s, and then cooled to ambient temperature at a cooling rate of 6.8 °C/s. To simulate the ICCGHAZ microstructures, the samples were subjected to thermal cycles simulating a double-pass welding. During the second thermal cycle, the samples were reheated at 130 °C /s up to 800 °C, maintained for 1 s at this temperature, and cooled to ambient temperature at a cooling rate of 6.8 °C/s, when the first thermal cycle similar to that used for the CGHAZ microstructure was finished. 10 mm × 10 mm × 71 mm rectangular samples of an X100 pipeline steel were prepared for thermal simulation. The simulated HAZs of ca. 10 mm in length were loacated in the middle of the samples, while the remaining parts of the samples were water-cooled to keep their original microstructure unaltered. The samples used for the corrosion studies were cubes with of 10 mm side cut from the center of the HAZs of the thermal simulation samples. The cutting surface (10 mm × 10 mm) in the middle of the HAZs was used as the working surface during the electrochemical experiments, while the surface formed by the simulated HAZs and the base steel zones (10 mm × 5 mm each) was used to observe the corrosion morphology. The base steel samples were cut in the form of 10 mm × 10 mm × 5 mm pieces with a surface area of 10 mm × 10 mm to form the working surfaces. All samples used for electrochemical experiments were soldered to copper wires on the back and embedded in an epoxy resin except for the working surfaces. The non-working surfaces of the samples used for morphology observation were sealed with waterproof insulating tape and silicone. Prior to the experiments, all working surfaces were wet ground sequentially up to 1500 grit with waterproof emery papers, sequentially cleaned with acetone, alcohol, and distilled water, and dried with cool air.

The test solution used for this research was a simulated Korla alkaline soil solution containing [21]: 0.2442 g/L $CaCl_2$, 3.1707 g/L NaCl, 2.5276 g/L Na_2SO_4, 0.6699 g/L $MgCl_2•6H_2O$, 0.2156 g/L KNO_3, 0.1462 g/L $NaHCO_3$ made from analytic grade reagents and deionized water. The pH of the solution was adjusted to 9.13 by adding NaOH and acetic acid solutions.

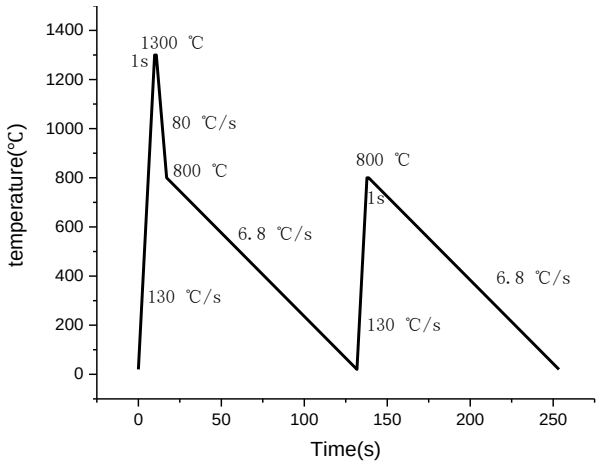

Figure 1. Cycle temperature curves used for the thermal simulation by Gleeble

2.2 Experimental methods

Open circuit potential (OCP) measurements were carried out for 7 h for each sample at intervals of about half an hour on a high-precision digital multimeter (FLUKE 289C) provided with a saturated calomel electrode (SCE, +0.241 V vs SHE). The potential used in this study was relative to SCE. The potentiostat used was a Solartron 1260/1287 (Hampshire, UK) Versastat device controlled by the accompanying corrware V3.10 software. This setup was used to determine the potentiodynamic polarization curves and to carry out electrochemical impedance spectroscopy (EIS) measurements on an X100 steel electrode (working electrode) with SCE and a platinum plate serving as reference and counter electrodes, respectively. Potentiodynamic polarization sweeps were carried out at a scan rate of 1 mV/s. EIS measurements were carried out under open circuit potential conditions with a sinusoidal potential excitation of 10 mV amplitude over a frequency range of 0.01–10 kHz. The potentiodynamic test results were analyzed with OriginPro2017, while the EIS results were analyzed and fitted to equivalent circuits using ZSimpWin V3.60.

Microstructural observations on the base steel and HAZs were carried out on a Zeiss Stereo optical microscope (OM) after etching the samples with 4% Nital (i.e., a mixture of 4 mL nitric acid and 96 mL ethanol). After exposure to the testing environment for 40 h, the corrosion products formed on the steel surface were removed carefully by both mechanical and chemical methods according to ASTM G1-03. Light scraping and scrubbing were used to remove the tightly adhered corrosion products, and a descaling solution (500 mL HCl, 3.5 g hexamethylenetetramine, and 500 mL distilled water) was used as a chemical removal procedure. The surface corrosion morphologies of the samples were observed by scanning electron microscopy (SEM, Hitachi S-3400N).

3. RESULTS AND DISCUSSION

3.1 Microstructure

The optical microstructure of the CGHAZ, ICCGHAZ, and base steel are presented in Fig. 2. In the case of the CGHAZ (Fig. 2a), the base steel was affected by a single thermal cycle with a peak

temperature of 1300 ºC. As a result, the prior austenite grains in the CGHAZ showed clearly visible boundaries and were coarse. These grains showed a microstructure is primarily formed by granular bainite and degenerate upper bainite [22]. The ICCGHAZ (Fig. 2b) was the intercritical region (Ac1−Ac3) obtained by reheating CGHAZ with a second thermal cycle. Prior austenite grain boundaries were the preferred nucleation sites for the reverted structure. Therefore, the matrix microstructure of the ICCGHAZ mainly consisted of degenerate upper bainite, granular bainite, and a small fraction of lumpy ferrite. A continuously distributed M/A constituent was formed along the coarse prior austenite grain boundaries (i.e., phase transformation). As shown in Fig. 2c, the microstructures of the base steel mainly consisted of granular bainite with minor fractions of ferrite structure.

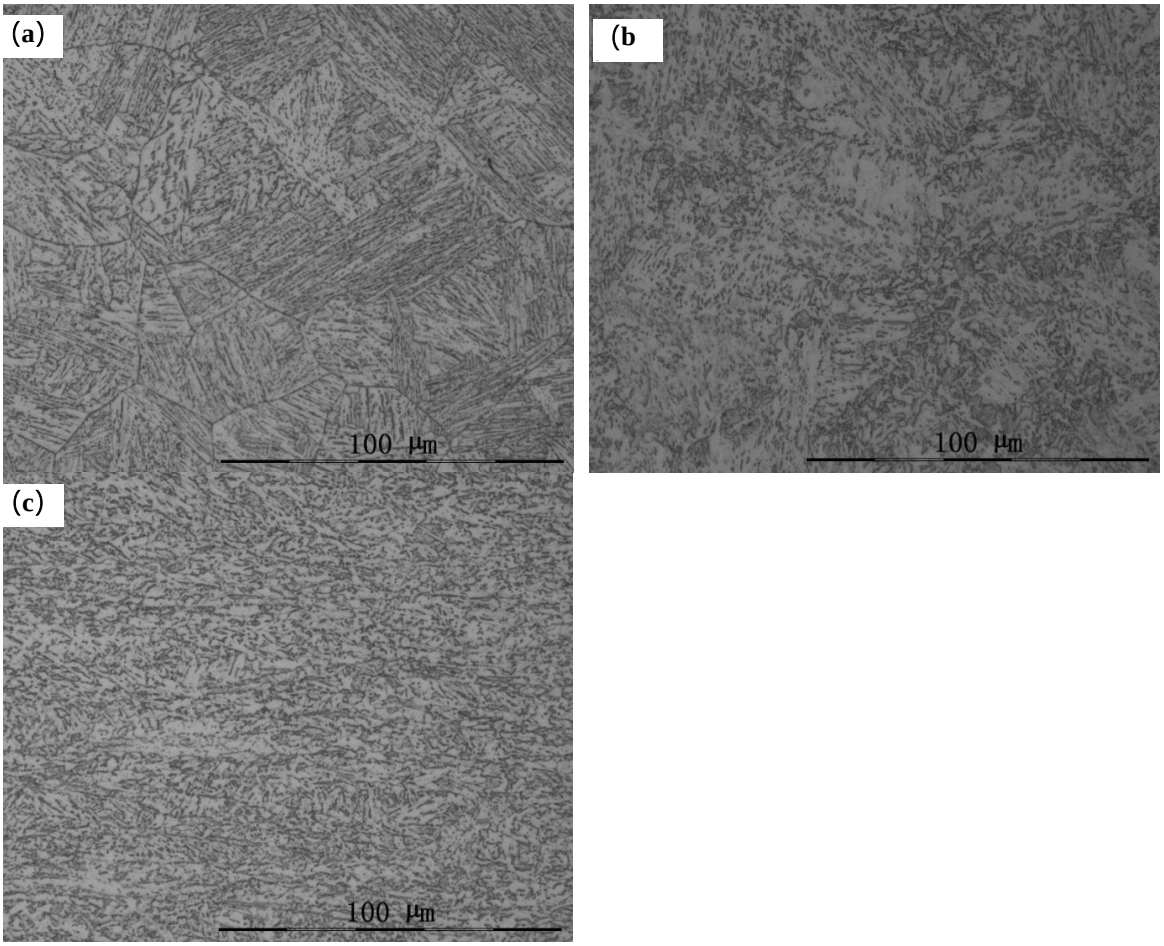

Figure 2. Optical microstructure of: (a) CGHAZ, (b) ICCGHAZ, and (c) base steel.

3.2 Electrochemical characterization

3.2.1 OCP

The OCP time dependence of the CGHAZ, ICCGHAZ, and base steel is shown in Fig. 3. All samples showed similar OCP–time profiles. The OCP decreased rapidly within the first 0.5 h, and this decrease moderated to finally levels off after 4.5 h. In this study, the OCP stabilization time was longer compared to previous reports on pipeline steel [10,13,14]. This can be mainly explained by the complex

composition of the soil simulated solution, which increased the time required to form a stable corrosion product film on the surface. After immersing the samples for 1.5 h, the base steel and the ICCGHAZ showed the most positive and negative OCP values, respectively, which is in line with the OCP distribution trend of X60–X80 pipeline steels [10–14]. The difference of OCPs revealed higher thermodynamic stability for the base steel compared to CGHAZ and ICCGHAZ, which can be explained by the more uniform microstructure of the X100 base steel [10].

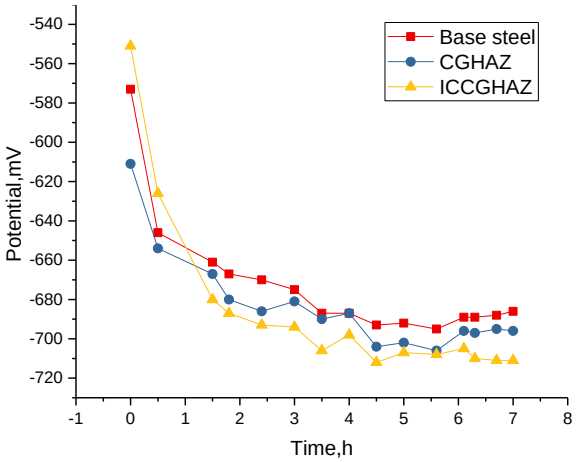

Figure 3. OCP vs immersion time for the samples immersed in a simulated alkaline soil solution.

2.2.2 Potentiodynamic polarization

Fig. 4 shows the potentiodynamic polarization curves of the CGHAZ, ICCGHAZ, and base steel materials under the conditions of the present study. The polarization curves of the CGHAZ, ICCGHAZ, and base steel immersed for 8 and 30 h in the soil simulation solution showed roughly similar characteristics: typical active dissolution and no passivation in the anode region. The corrosion of X100 pipeline steels in HCO_3^- [16, 17] and HCO_3^-+Cl^- [23] solutions has been previously reported to proceed with passivation behavior. NO_3^- can facilitate the formation of a passivation film [24], while SO_4^{2-} inhibited Cl^- corrosion [25]. However, the mechanism behind the absence of passivation in an X100 steel immersed in solution containing these anions needs to be further studied. The appearance of a "pseudo-passivation" platform in the anodic polarization zone of the ICCGHAZ immersed for 8 h from -0.62 to -0.74V was attributed to the intersection of the cathodic currents of the oxygen reduction reaction (Eq. (1)) with the anode current affected by the corrosion product film [16]. The cathode polarization region of the polarization curve below ca. -1 V was almost similar for base steel, CGHAZ, and ICCGHAZ, such that the three materials present mostly the same water reduction reaction activity (Eq. (2)). The diffusion control characteristics can be observed in the cathodic polarization zone with the oxygen reduction reaction of the CGHAZ soaked for 8 h, while other polarization curves with more negative potential or lower corrosion current densities did not show obvious diffusion control. The corrosion current densities extracted from the polarization curves are shown in Table 1. Among the materials tested herein, the base steel showed the lowest corrosion current density followed by CGHAZ and ICCGHAZ for two immersion times. The higher corrosion current density of CGHAZ compared to the base steel resulted from a more active local corrosion, which was favored by the inhomogeneity and the greater

number of lattice defects of the more rapidly cooled microstructure. The higher corrosion current density of ICCGHAZ was caused by the presence of irregular granular ferrite and M/A structure formed at the prior austenite grain boundaries, resulting in a more negative corrosion potential and a higher corrosion activity. The corrosion current densities of the samples immersed for 30 h were greater than those of the samples immersed for 8 h, in line with previous results [26, 27] dealing with the corrosion behavior of X100 pipeline steel in a simulated Korla soil solution. The corrosion rate increased at the initial stage of the corrosion process. The tiny particles of corrosion product formed on the surface of the samples at the initial stage of corrosion could have increased the area of the cathode reaction zones and therefore promote corrosion [27].

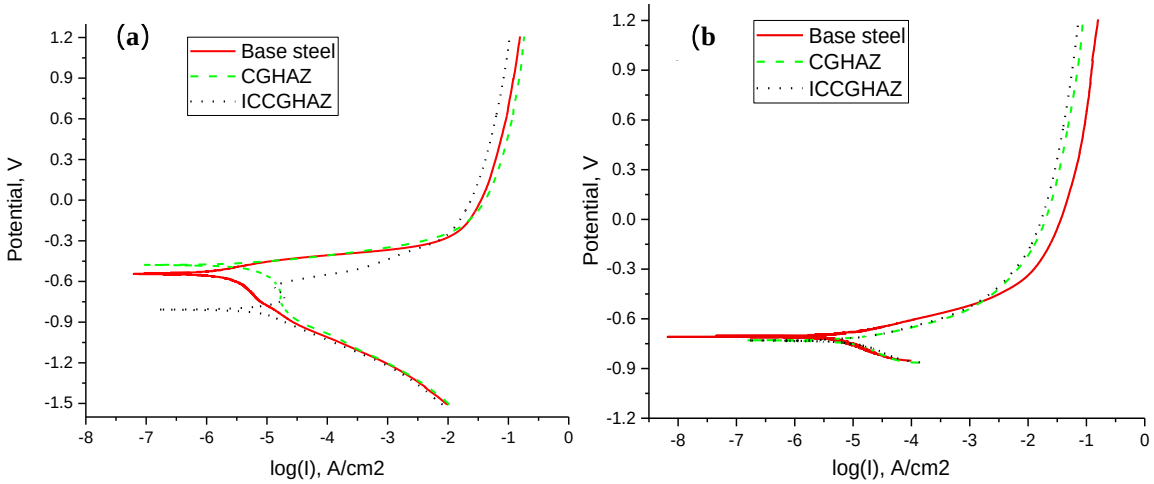

Figure 4. Polarization curves of the samples in a simulated alkaline soil solution for (a) 8 h and (b) 30 h

$$2H_2 + O_2 + 4e^- \rightarrow 4HO^- \quad (1)$$
$$2H_2O + 2e^- \rightarrow H_2 + 2HO^- \quad (2)$$

Table 1. Corrosion current densities estimated from the polarization curves

time/h	Corrosion current densities/(ηA/cm^2)		
	Base steel	CGHAZ	ICCGHAZ
8	2.37	3.35	3.88
30	3.13	6.76	7.22

2.2.3 EIS

Figs. 5 and 6 show the Nyquist plots and the phase Bode diagrams of EIS for X100 base steel, CGHAZ, and ICCGHAZ immersed in test solution for 8 and 30 h. As shown in the diagrams, the corrosion mechanisms and the nature of the interfacial interactions for the base steel, CGHAZ, and FGHAZ did not vary significantly with the immersion time [24]. The Nyquist diagrams revealed a capacitive reactance arc shrinking along the Z_{re}-axis direction in the low frequency range, indicating the

formation of a corrosion product film on the surface of the sample that altered the electrode reaction rate [8]. At the low frequency end, the EIS results of the samples immersed for 8 h show an irregular profile, which may be due to the intermediate corrosion products formed and the unstable surface morphology of the samples.

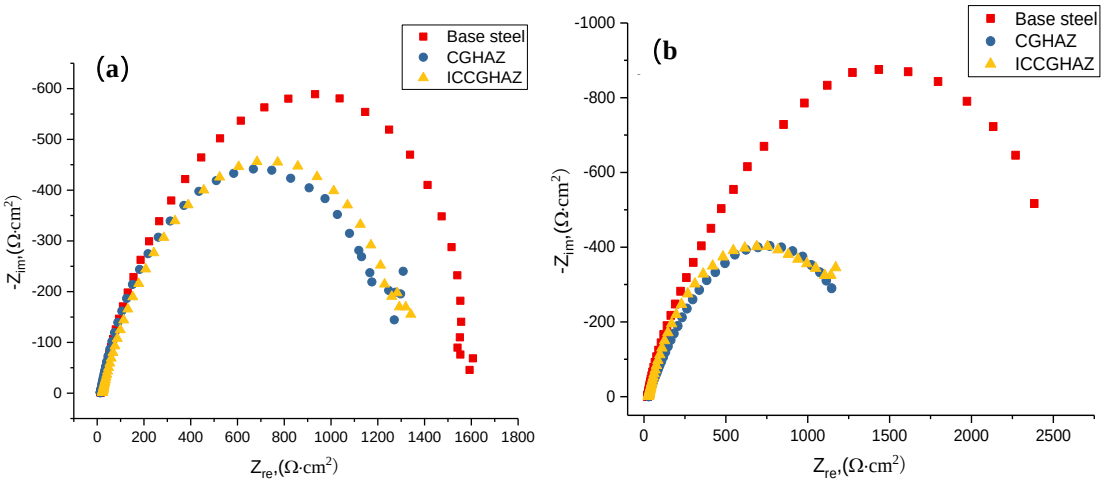

Figure 5. Nyquist plots of the base steel and HAZ in simulated alkaline soil solution for (a) 8 h (b) 30 h

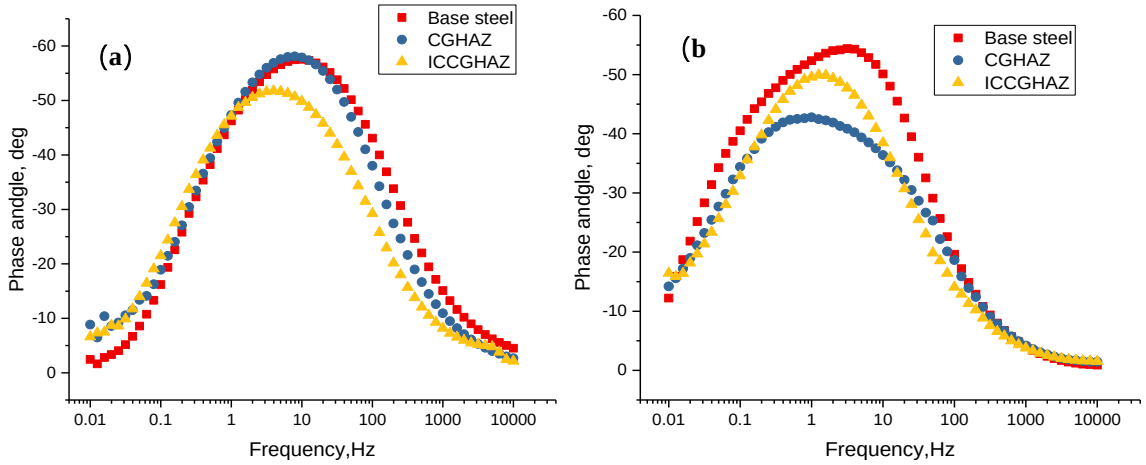

Figure 6. Bode plots of the base steel and HAZ in simulated alkaline soil solution for (a) 8 h (b) 30 h

The EIS curves of the samples immersed for 30 h showed no irregular disturbance at the low frequency end, although the curve of FGHAZ exhibited the Warburg impedance characteristic of diffusion of the charge carriers. For all the samples, the interface depicted from the Nyquist and Bode spectra, contained no more than two-time-constant [16]. Based on relevant works [13, 16, 29, 30] and comparing the error results fitted by Zsimwin software, the equivalent circuit depicted in Fig. 7(c) was used to fit the EIS data of the base steel immersed for 30 h. The equivalent circuit depicted in Fig. 7(b) was used to fit the EIS data of the ICCGHAZ immersed for 30 h. The equivalent circuit depicted in Fig. 7(a) was used to fit the remaining EIS data. The fitting results are listed in Table 2. As shown in Fig. 6

and Table 2, R_s represents the solution resistance, R_f is the corrosion product film resistance, R_{ct} corresponds to the charge transfer resistance of the corrosion process, while constant phase elements (CPE) Q_f and Q_{dl} represent non-ideality of the corrosion product film capacitance and the double layer capacitance at the metal/electrolyte interface, respectively, n_f and n_{dl} are the CPE exponents, and Z_w corresponds to the Warburg impedance.

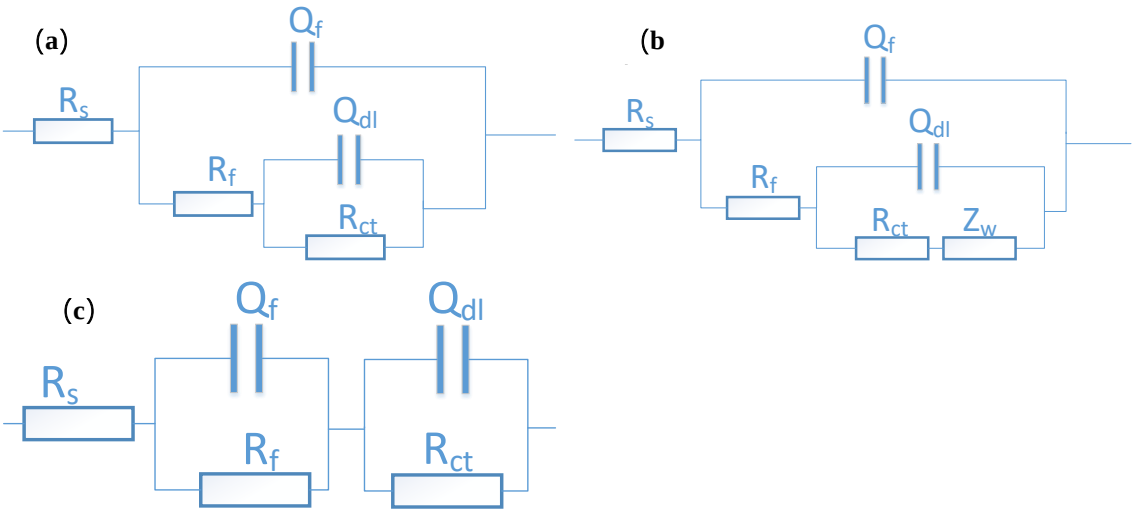

Figure 7. Equivalent circuit of the base steel and HAZ in a simulated alkaline soil solution

As revealed by the fitting results, the base steel showed the largest charge transfer resistance （Rct） and polarization resistance (R_f+R_{ct}) for both immersion times, followed by CGHAZ and ICCGHAZ. This was consistent with the polarization curve measurements. As the immersion time increased, the resistance and Q_f of the corrosion product film increased significantly, and the base steel showed the largest corrosion product film resistance and the lowest corrosion rate. This phenomenon can be explained by the corrosion product film formed on the surface of the base steel having a more uniform microstructure and being more compact.

Table 2. Equivalent circuit fitting for the EIS data

Time (h)	Microstructures	R_s (Ω•cm^2)	Q_f (Ss^n/cm^2)	n_f	R_{fs} (Ω•cm^2)	Q_{dl} (Ss^n/cm^2)	n_{dl}	R_{ct} (Ω•cm^2)	W (Ss^n/cm^2)	Chi-square
8	Base steel	14	1.811×10^{-4}	0.75	8	1.282×10^{-4}	0.74	1670	/	5.664×10^{-4}
	CGHAZ	10	1.332×10^{-4}	0.31	14	3.913×10^{-4}	0.77	1453	/	2.288×10^{-4}
	ICCGHAZ	20	6.871×10^{-5}	0.71	3	4.856×10^{-4}	0.72	1407	/	2.044×10^{-4}
30	Base steel	23	6.716×10^{-4}	0.74	346	1.426×10^{-3}	0.82	2280	/	1.906×10^{-4}
	CGHAZ	28	6.716×10^{-4}	0.74	144	1.026×10^{-3}	0.62	1280	/	6.056×10^{-5}
	ICCGHAZ	27	9.082×10^{-4}	0.71	30.4	2.890×10^{-4}	0.72	1184	2.2×10^{-2}	3.415×10^{-5}

2.3 Corrosion morphologies

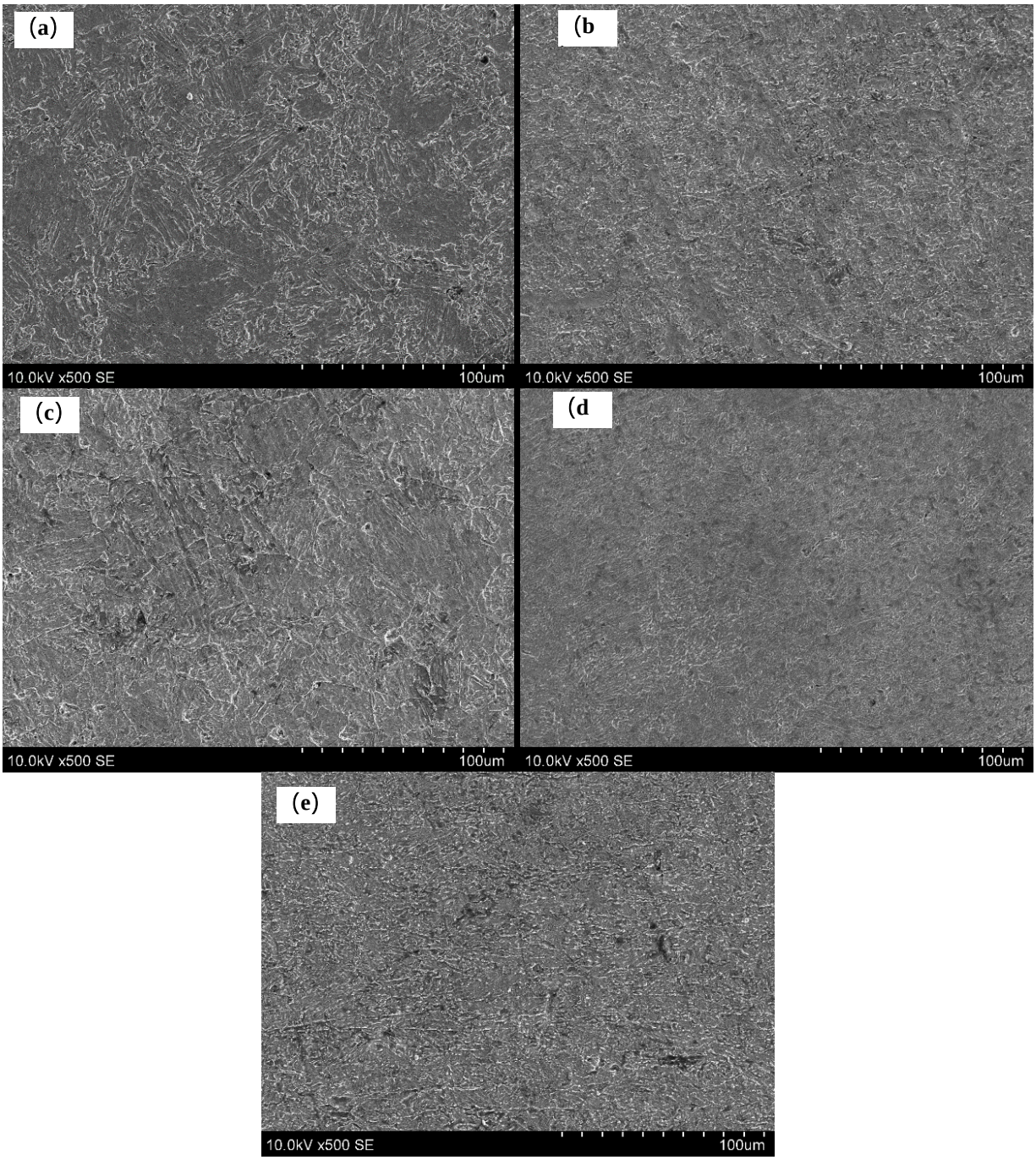

Figure 8. SEM Surface micrographs of: (a) CGHAZ, (b) base steel adjacent to CGHAZ, (c) ICCGHAZ, (d) base steel adjacent to ICCGHAZ, and (e) base steel.

The steel surface corrosion morphologies after immersion in the test solution for 40 h are shown in Fig. 8. The HAZ connected with the base metal presented serious corrosion, while the base metal underwent slight corrosion (i.e., galvanic corrosion). The extent of the corrosion process followed the trend: HAZ > base steel > base steel adjacent to the HAZ. Corrosion on ICCGHAZ was slightly more

intense than on CGHAZ, but this difference was lower than that between HAZ and base steel. The corrosion micromorphology was completely consistent with the electrochemical experiment results, indicating that the effects of the welding thermal cycles on the corrosion behavior and resistance were complex and important.

4. CONCLUSIONS

(1) The microstructures of CGHAZ and ICCGHAZ simulated from X100 pipeline steels by Gleeble thermal simulator with different peak temperatures, cooling rates, and cycle times differed significantly from that of the base metal. The microstructure of the base steel was uniform and mainly composed of granular bainite. The microstructure of the CGHAZ contained obvious grain boundaries and coarse grains and consisted primarily of granular bainite and degenerate upper bainite. The microstructure of ICCGHAZ was also mostly formed by degenerate upper bainite and granular bainite, although the M/A island structure is distributed at the grain boundary.

(2) The base steel, CGHAZ, and ICCGHAZ of the X100 pipeline steel showed typical active dissolution characteristics in a simulated Korla alkaline soil solution.

(3) The results of electrochemical analysis revealed the X100 base steel to present highest thermodynamic stability, the lowest corrosion current density, and the highest polarization resistance in simulated Korla alkaline soil solution among the materials tested herein. ICCGHAZ had the lowest thermodynamic stability, the largest corrosion current density, and the lowest polarization resistance. CGHAZ showed an intermediate behavior.

(4) SEM surface micrographs revealed galvanic corrosion on the samples containing HAZ and base steel. The HAZ immersed in a simulated Korla alkaline soil solution was corroded to a larger extent compared to the base steel.

References

1. B. Zhang, C. Qian, Y. Wang, Pet. Eng. Constr., 38 (2012) 1.
2. Y.C. Chen, X.H. Wang, C. Wang, Surf. Technol., 47(2018)218
3. X.D. Li，X. Li，S.X. Wang，S.B. Hu, Q.K. He, J.H. Liu, *Heat Treat. Met.*, 42(2017)66.
4. R. Ghajara, G. Mironeb, A. Keshavarza. Mater. Des., 43(2013)513.
5. J. Johnson, M. Hudson, N. Takahashi, M. Nagase, A. Yamamoto, ASME. International Pipeline Conference, 2008 7th International Pipeline Conference, Calgary, Alberta, Canada, 2008, 453.
6. G.L. Wang, W. Guan, J.K. Han, *Pet. Plan. Eng.*, 26(2015)1.
7. C.W. Du,Z.Y. Liu, P.Liang, G.F. Jia, X.G. Li, *Heat Treat. Met.*, 33(2008)80.
8. M.Wu, F. Xie, X. Chen，D. Wang, *J. Sichuan Univ.(Eng. Sci. Ed.)*, 45(2013)185.
9. G. Papadakis, *J. Loss Prevent. Proc.*, 12(1999)91.
10. C.H. Liu, W. Liu, M.X. Lu, *Corros. Sci. Prot. Technol*., 20(2008)206.
11. Z. Fan, J.Y. Liu, S.L. Li, *J. Southwest Pet. Univ.(Sci. Tech. Ed.),* 31(2009)171.
12. F. Mohammadi, F. F. Eliyan, A. Alfantazi, *Corros. Sci*., 63(2012)323.
13. W. Zhao, Y. Zou，Z.D, Zou，K. Matsuda, *Int. J. Electrochem. Sci*., 10 (2015) 9725.
14. C.W. Shi, Y.B. Zhang, P. Liu, Y.L. Xie, *Int. J. Electrochem. Sci*., 13 (2018) 2412.
15. M. Zhang, L. Li, K.K. Cheng, *Ordnance Mater. Sci. Eng*., 41(2018)1.

16. F. F. Eliyan, A. Alfantazi, *Corros. Sci*., 74(2013) 297.
17. F. F. Eliyan, F. Icre and A. Alfantazi, *Mater. Corros*., 65(2014)1162.
18. L.Z. Zhang, X.L. Xu, F.P. Zhang, X.Y. Li, G. Li, *Hot Work. Tech*., 44(2015)67.
19. X.L.Wang, X.M.Wang, C.J.Shang, R.D.K.Misra, *Mater. Sci. Eng*. A, 649(2016) 282.
20. P. Mohseni, J.K. Solberg, M. Karlsen, *Metall. Mater. Trans*. A, 45A(2014)384.
21. P. Liang, C.W. Du, X.G. Li, *J. Chin. Soc. Corros. Prot*., 31(2011)97.
22. X.D. Li, X.P. Ma, S. V. Subramanian, *Int. J. Fract*., 193(2015)131.
23. Y. Zhao, P. Liang, Y.H. Shi, *J. Chin. Soc. Corros. Prot*., 35(2015)113.
24. J.S. Lu, J.Y. Zhang, J. Zhejian *Univ. Technol*., 25(1997)16.
25. Z.Q. Shi，X.Y. Zhang，Y.F. Wang, *J. Chin. Univ. Pet.(Nat. Sci. Ed.),* 40(2016)128.
26. H.H. Li, C.M. Xu, *Mater. Mech.Eng*., 38(2014)75.
27. X.Y. Zhang, Z.Q. Shi, Y.F. Wang, *J. Chin. Soc. Corros. Prot*., 35(2015)33.
28. G. Khalaj, M.J. Khalaj, *Int. J. Pres. Vessel. Pip*., 145(2016)1.
29. R. Cabrera-Sierra, I. Garia, E. Sosa, T. Oropeza, I. Gonzalez, *Electrochim. Acta*, 46(2000)487.
30. X.H.Wang, Z.Q. Wang, Y.C. Chen, *Surf. Technol*., 47(2018)142.